applied sciences

MDPI

Article

Simulation of Full Wavefield Data with Deep Learning Approach for Delamination Identification

Saeed Ullah [1], Pawel Kudela [1,*], Abdalraheem A. Ijjeh [1,2], Eleni Chatzi [3] and Wieslaw Ostachowicz [1]

[1] Institute of Fluid Flow Machinery, Polish Academy of Sciences, 80-231 Gdansk, Poland; sullah@imp.gda.pl (S.U.); aijjeh@us.es (A.A.I.); wieslaw@imp.gda.pl (W.O.)
[2] GRVC Robotics Laboratory, University of Seville, 41092 Seville, Spain
[3] Department of Civil, Environmental, and Geomatic Engineering, ETH Zurich, 8093 Zurich, Switzerland; chatzi@ibk.baug.ethz.ch
* Correspondence: pk@imp.gda.pl

Abstract: In this work, a novel approach of guided wave-based damage identification in composite laminates is proposed. The novelty of this research lies in the implementation of ConvLSTM-based autoencoders for the generation of full wavefield data of propagating guided waves in composite structures. The developed surrogate deep learning model takes as input full wavefield frames of propagating waves in a healthy plate, along with a binary image representing delamination, and predicts the frames of propagating waves in a plate, which contains single delamination. The evaluation of the surrogate model is ultrafast (less than 1 s). Therefore, unlike traditional forward solvers, the surrogate model can be employed efficiently in the inverse framework of damage identification. In this work, particle swarm optimisation is applied as a suitable tool to this end. The proposed method was tested on a synthetic dataset, thus showing that it is capable of estimating the delamination location and size with good accuracy. The test involved full wavefield data in the objective function of the inverse method, but it should be underlined as well that partial data with measurements can be implemented. This is extremely important for practical applications in structural health monitoring where only signals at a finite number of locations are available.

Keywords: lamb waves; structural health monitoring; surrogate modeling; delamination identification; deep learning; autoencoders; ConvLSTM

Citation: Ullah, S.; Kudela, P.; Ijjeh, A.A.; Chatzi, E.; Ostachowicz, W. Simulation of Full Wavefield Data with Deep Learning Approach for Delamination Identification. *Appl. Sci.* **2024**, *14*, 5438. https://doi.org/10.3390/app14135438

Academic Editor: Raffaele Zinno

Received: 23 May 2024
Revised: 18 June 2024
Accepted: 21 June 2024
Published: 23 June 2024

1. Introduction

Detecting delamination in composite materials poses a significant challenge for conventional visual inspection techniques, as it occurs between the plies of the composite laminate and remains invisible from external surfaces [1,2]. As a result, various nondestructive testing (NDT) and structural health monitoring (SHM) techniques have been proposed for delamination identification in composite structures. Among these techniques, ultrasonic guided waves are widely recognized as one of the most promising approaches for quantitatively identifying defects in composites [3,4]. Their extensive application is attributed to their high sensitivity to small defects, low propagation attenuation, and ability to monitor large areas using only a small number of sparsely distributed transducers [5–7].

However, using a smaller number of transducers does not make it possible to obtain high-quality resolution damage maps and accurately asses the size of the experienced damage. Conversely, employing a very dense array of transducers is impractical in most situations. To address these issues, a scanning laser Doppler vibrometer (SLDV) can be employed. An SLDV can measure the propagation of guided waves in a highly dense grid of points over the surface of a large specimen, which is often termed as a full wavefield. In recent years, full wavefield signals have been utilised for detecting and localising defects in composite structures [8–10]. These damage identification techniques using full wavefield signals can effectively estimate not only the location but also the size of the damage [9].

In our previous works [8,11], full wavefield data were directly processed to obtain damage maps. Here, full wavefield data are used to train a deep learning (DL) model for predicting guided wave interactions with defects. Such a DL model has wider potential application, including cases when sparse data are available.

Full wavefield scans offer valuable insights into the interaction of guided waves with defects. However, acquiring the full wavefield of guided waves is a time-consuming process.

Furthermore, the damage identification methods operating on the full wavefield cannot be directly extended to the cases when only spatially sparse data are available, e.g., an array of sensors is installed on the structure. In such a case, usually, an inverse procedure is employed in which efficient methods for solving wave equations are required. However, the numerical modelling of ultrasonic guided wave propagation in solid media exhibiting discontinuities, such as damage, is complex; it requires fine discretisation and is computationally intensive. Even though methods such as the p-version of the finite element method (p-FEM) [12], the isogeometric analysis (IGA) [13] approach, the spectral cell method (SCM) [14], and the time domain spectral element method (SEM) [15] are more efficient and accurate than the classical FEM with linear elements, they are not efficient enough to be used in inverse methods (about half the number of nodes is required to obtain the same accuracy according to [16]). In the end, calling the objective function for each damage case scenario in which the forward solver is used is unfeasible, because computations for even a simple plate can take up to 1 h.

An alternative approach is to utilise a surrogate model for generating full wavefield data or time series-resembling signals registered at an array of sensors. A surrogate model imitates the behaviour of the simulation model while replacing time-consuming forward simulations with approximate solutions. It can be based on DL, as well as physics-informed, neural networks [17,18].

DL has seen extensive research and successful implementation in the fields of NDT and SHM. The convolutional neural network (CNN) is among the most popular DL architectures. Initially introduced for image processing, the CNN has now been extended to various research domains, including NDT and SHM applications such as damage detection, localization, and characterisation [19–21].

In modern DL, the focus is on constructing more efficient and streamlined architectures, wherein key components are accentuated, and essential attributes from the original data are preserved. This process of crafting architectures involves the meticulous extraction of feature representations from data, which is commonly referred to as feature engineering. However, this practice demands specialised knowledge and a significant investment of time. Moreover, the intricacies of feature engineering differ across various data types, thus posing a challenge in establishing universally applicable procedures.

An established option for feature extraction, alleviating feature engineering, is delivered in the form of an autoencoder, a type of neural network that possesses the capability to autonomously learn features from unlabeled data using unsupervised learning techniques. This unique ability obviates the need for extensive feature engineering [22–24]. Consisting of two integral components: an autoencoder comprises an encoder responsible for mapping inputs to a desired latent space and a decoder that skilfully reverts the latent space back to the original input domain. By harnessing appropriately curated training data, autoencoders have the capacity to generate a latent representation, thereby negating the necessity for labour-intensive feature engineering endeavours.

However, general autoencoders may not capture spatial features, such as images, or sequential information when dealing with dynamics, like time series forecasting. To address the limitation of capturing spatial features, the use of a CNN-based autoencoder is recommended, whereas, an RNN-based autoencoder is usually employed for learning features from time series data. Deep CNN-based autoencoders (DCAEs) excel at extracting spatial features from image-based input data, they may not be sufficient for extracting features from sequences of images, particularly in cases involving full wavefield data, which contain numerous sequential frames/images for each delamination scenario. For such situations, ConvLSTM [25] is employed. ConvLSTM combines CNN and LSTM, thus enabling it to effectively learn features from sequences of images. In ConvLSTM architecture, the CNN is responsible for learning features from images, while LSTM retains sequential information.

DCAE-based surrogate modelling has been implemented in [26,27]. Jo et al. [26] developed a DCAE framework for the purpose of extracting latent features from spatial properties and investigating adaptive surrogate estimation to sequester CO_2 into heterogeneous deep saline aquifers. They used a DCAE and a fully convolutional network for reducing the computational costs and extracting dimensionality-reduced features for conserving spatial characteristics. Nikolopoulos et al. [27] presented a nonintrusive DL-based surrogate modelling scheme for the predictive modelling of complex systems, which they described using parametrized time-dependent partial differential equations.

Recently, Peng et al. [28] proposed an encoding convolution long short-term memory (encoding ConvLSTM) framework for building a surrogate structural model with spatiotemporal evolution, thus estimating structural spatiotemporal states and predicting dynamic responses under future dynamic load conditions. Zargar and Yuan [29] presented a hybrid CNN–recurrent neural network (RNN) for handling spatiotemporal information extraction challenges in impact damage detection problems.

Inspired by the successful implementations of CNN and RNN for the representation of spatiotemporal dynamics, we explore for the first time the potential of deep neural networks for the modelling of complex behaviour of guided waves interacting with defects.

Therefore, in this work, the damage identification method that relies on the anomalies of propagating guided waves is employed. It is an inverse method in opposition to the most commonly used data-driven methods. The most significant contribution of this work is the development of a deep ConvLSTM autoencoder-based surrogate model. The main function of the developed model is to capture and learn the full wavefield representation—the animation of propagating waves, their reflections from boundaries and defects, waveform entrapment at the delamination, etc. Subsequently, it transforms this information into a compressed domain known as the latent space. Separate training is performed for the encoder so that inputs containing both reference frames (without delaminations) and an image showing the shape and location of the delaminations are only needed to restore the full wavefield of guided waves interacting with presented defects. The inference of the DL model replaces the solver of the system's governing equations, i.e., the forward modelling step in the inverse method, thus resulting in significant time and computational cost savings.

The novelty of this research lies in the proposed architecture of a deep ConvLSTM-based autoencoder, as well as its utilisation in the inverse procedure for delamination identification. The particle swarm optimisation (PSO) approach was selected and applied [30] in the inverse procedure.

2. General Concept

A framework of the proposed inverse method for damage identification is shown in Figure 1. It is composed of three building blocks: (i) dataset computation, (ii) supervised learning, and (iii) inverse method.

For the problem of guided wave-based damage identification, it is infeasible to collect a large experimental dataset that would cover various damage case scenarios, because it would require manufacturing and damaging multiple samples. Therefore, a possible alternative is a dataset computed numerically by using, e.g., a finite element solver. In particular, the dataset that is employed in the current research was generated by using the time domain spectral element method [15]. The dataset focuses on delamination as the most dangerous type of damage occurring in composite laminates such as carbon fibre-reinforced polymers (CFRP). Delamination is a separation between plies of composite laminate and can be a result of impact or manufacturing process. Delamination is often not visible from the outside and can grow during the operation of the structure. The process of generating this dataset involved modelling a square plate with delaminations of varying shapes and positions into the parametric unstructured mesh. Following this, a forward solver was utilised to capture the interactions between the propagating guided waves with the delamination and the boundaries of the plate. It resulted in 512 frames for each delamination scenario. The dataset has been made available online [31] so that the results can be easily replicated.

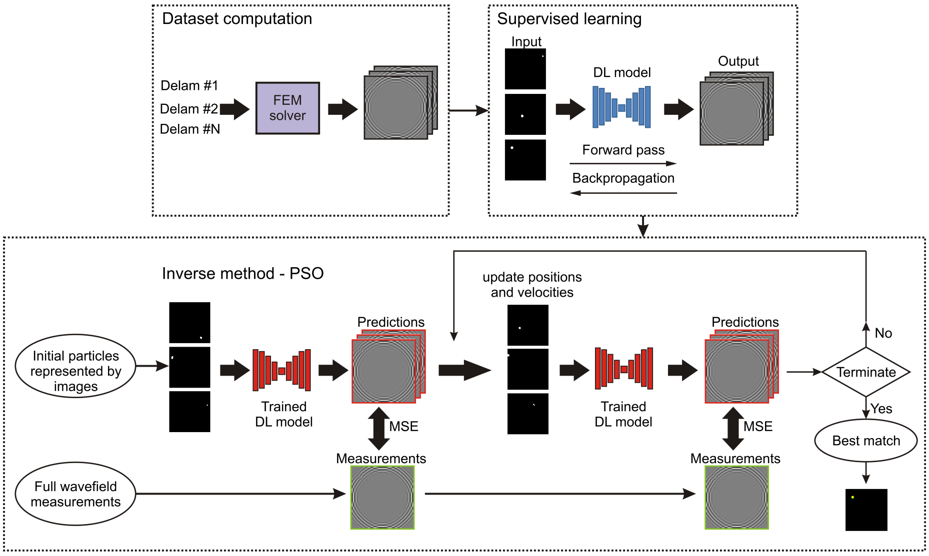

Figure 1. Flowchart of the proposed inverse method for damage identification.

The dataset was used for the supervised training of the DL model. The idea was to input to the DL model a binary image in which ones (white pixels) represent the delamination region and zeros (black pixels) represent the healthy region for the respective delamination cases. Once the model is trained, it can be used in the inverse procedure as a surrogate model instead of a computationally expensive p-FEM or SEM forward solver.

It should be noted that the PSO algorithm was used in the inverse method due to its efficiency in handling more general formulations of objective functions (as opposed to stricter algebraic constructs), but other algorithms can be used as well. On one hand, the inputs are initial particles represented by binary images in Figure 1. These are fed to the trained DL model, which, in turn, is predicting the full wavefield of propagating waves for respective delamination scenarios. On the other hand, full wavefield measurements are acquired. An objective function is built upon the computation of the mean square error (MSE) between the predicted wavefield and the measured wavefield. Next, the particle positions and their velocities are updated accordingly until the termination criterion is met. Finally, the identified delamination is visualised for the best match. It should be added that the proposed method was validated on synthetic data only.

The next sections describe each building block of the proposed method in detail.

3. Dataset Computation and Preprocessing

Essentially, the computed dataset resembles the particle velocity measurements at the surface of the plate acquired by the SLDV in the transverse direction as a response to the piezoelectric transducer (PZT) excitation placed on the surface of the plate in the centre. The scheme of the setup is presented in Figure 2.

3.1. Dataset Computation

A synthetic dataset of propagating waves in carbon fibre-reinforced composite plates was computed by using the parallel implementation of the time domain SEM [15]. The model is based on the Mindlin–Reissner theory of plates, which means that five degrees of freedom are available at each node, namely three translational displacements and two rotational displacements.

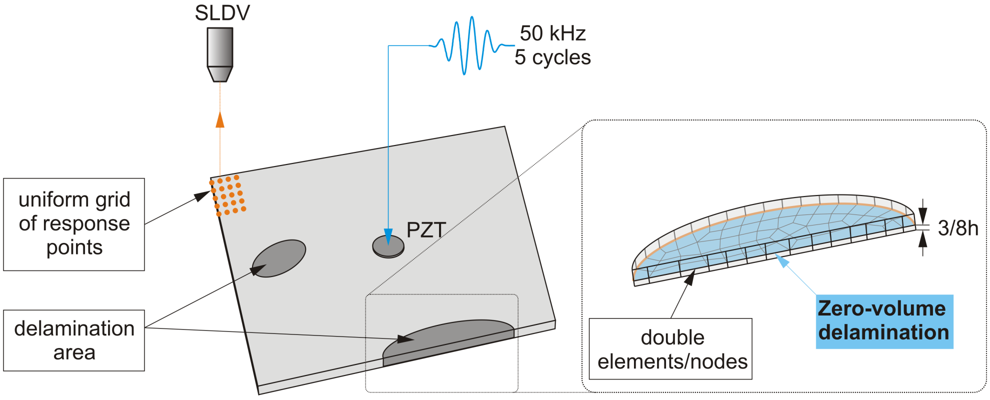

Figure 2. Numerical and experimental setup showing the types of possible delaminations (embedded and opened at the edge), piezoelectric transducer (PZT), and scanning laser Doppler vibrometer (SLDV).

The input signal was a five-cycle Hann window-modulated sinusoidal tone burst. The carrier frequency was assumed to be 50 kHz. The total wave propagation time was set to 0.75 ms. The number of time integration steps was 150,000, which was selected for the stability of the central difference scheme. It should be added that the PZT was not fully modelled. The excitation was applied in the form of equivalent piezoelectric forces. Additionally, the stiffness and mass were modified in plate elements corresponding to the PZT position.

The material was a typical cross-ply CFRP laminate. The stacking sequence $[0/90]_4$ was used in the model. The delamination was modelled between the third and fourth lamina at 3/8 of the total thickness. The properties of a single ply were as follows [GPa]: $C_{11} = 52.55$, $C_{12} = 6.51$, $C_{22} = 51.83, C_{44} = 2.93, C_{55} = 2.92, C_{66} = 3.81$. The assumed mass density was 1522.4 $\mathrm{kg/m^3}$. These properties were selected so that the wavefields simulated numerically would match the wavefields measured by the SLDV on real CFRP specimens. The wavelength of the dominating A0 Lamb wave mode was 21.2 mm. This information was utilised for the automatic generation of unstructured meshes so that at least 10 nodes per wavelength were obtained.

A total of 475 cases were simulated, thus representing Lamb waves propagation and interaction with single delamination for each case. The following random factors were used in the simulated delamination scenarios:

- The coordinates of the centre of delamination;
- The delamination geometrical size determined by the ellipse minor and the major axis randomly selected from the range 10–40 mm;
- The delamination angle randomly selected from the range 0°–180°.

An embedded MATLAB function was used for randomisation. However, the coordinates of the centre of delamination very close to the PZT were excluded. It should be added that two types of delamination, as shown in Figure 2, were possible, namely fully embedded or opened at the edge. The delamination modelling was realised by writing custom geometry files, which were used to generate an unstructured mesh consisting of quadrilateral elements by using GMSH software [32] (one mesh per delamination scenario). An exemplary mesh of quadrilateral elements is shown in Figure 3 in which the green elements highlight the delamination, whereas the red elements represent the location of the piezoelectric actuator. Next, the mesh was modified by doubling elements and splitting nodes at the delamination region. This resulted in the so-called zero-volume delamination. Next, the quadrilateral elements were converted to 36-node spectral elements by using a custom MATLAB script. The wave propagation problem was solved using an in-house code of the time domain SEM, which was run on the GPU. The obtained animations of the propagating guided waves were converted to images (frames).

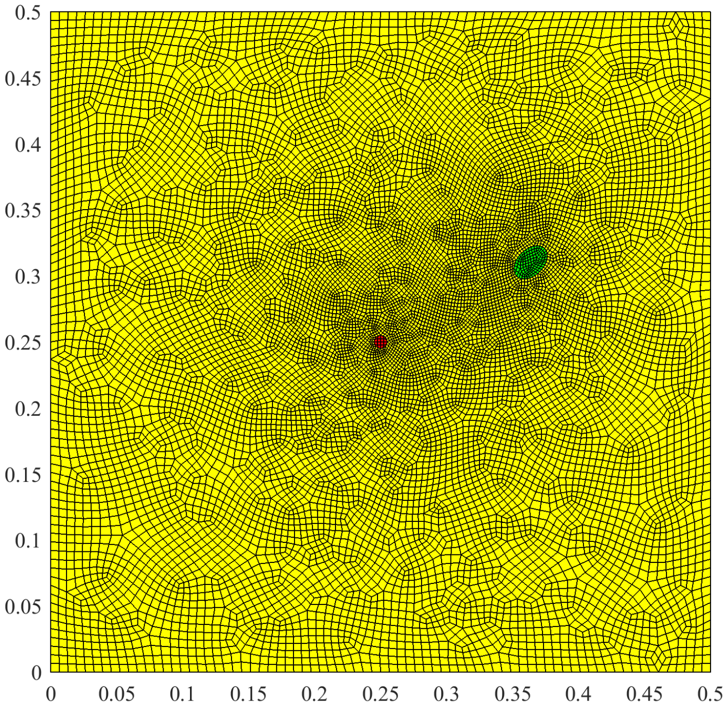

Figure 3. An exemplary mesh containing piezoelectric transducer (red) and random delamination (green) used for Lamb wave propagation modelling.

The dataset contains 475 different delamination cases, with 512 frames per case, thus producing a total number of 243, 200 frames with a frame size of (500×500) pixels representing the geometry of the specimen surface of size (500×500) mm^2. The frames in the dataset are 8-bit .png greyscale images. As was mentioned before, the dataset has been made available online [31].

In the current DL model implementation, the spatial size of the wavefield was further downsampled to (256×256) for the purpose of reducing the computational complexity.

It is important to note that input data to the DL model in the form of the binary image representing the respective delamination case (as it is presented in Figure 1) was insufficient to train a reliable model. It was necessary to provide additional inputs in the form of reference full wavefield frames (without delaminations). This is explained, along with the DL model, in Section 4.

3.2. Data Augmentation

The best approach for improving the generalisation capabilities of the neural network is to acquire more data. However, in practice, it can be difficult to acquire more data, and the amount of available data for neural network training is limited. In order to tackle this issue, one approach is to create some fake data based on the original dataset and add them to the training set, which is termed data augmentation. Data augmentation is an efficient approach for various computer vision and DL tasks. Data augmentation includes randomly cropping a region from the original image, adjusting the contrast, rotation for a small angle and flipping images, etc. [33]. In this research work, the dataset is composed of 475 delamination cases, which are not enough for a targeted DL model to perform well. Therefore, all the images in the 475 delamination cases were flipped diagonally, horizontally, and vertically in order to enhance the performance of the proposed DL model. Therefore, the total dataset after data augmentation is now composed of 1900 $(475 \times 4 = 1900)$ delamination cases.

3.3. Dataset Division and Preprocessing

For the training and evaluation of the proposed DL model, the dataset was divided into two sets: training and testing, with a ratio of 80% and 20%, respectively. Moreover, 20% of the training set was preserved as a validation set to validate the model during the training process.

Moreover, the dataset was normalised to a range of $(0, 1)$ to improve the convergence of the gradient descent algorithm. Due to memory limitations, 32 consecutive frames in each delamination case were selected for DL model training. Additionally, the frames displaying the propagation of guided waves before interaction with the delamination had no features to be extracted. Hence, only a certain number of frames were selected from the initial occurrence of the interactions with the delamination.

4. The Proposed DL Model for Supervised Learning

In this research work, we developed a novel deep ConvLSTM autoencoder-based surrogate model utilising full wavefield frames of Lamb wave propagation for the purpose of data generation for delamination identification in thin plates made of composite materials. The developed DL model takes as an input of 32 frames without delamination (reference frames) representing the full wavefield and the delamination information of the respective delamination case in the form of binary images for the purpose of producing the full wavefield propagation of Lamb waves through space and time (3D matrix). The most important aspect of the DL model is the prediction of the interaction of Lamb waves with the delamination so that the delamination location, shape, and size can be estimated.

The complete flowchart of the proposed DL model is presented in Figure 4. The training and evaluation process of the proposed model can be summarised in the following three steps:

1. **Feature extraction:** As we have no labels for the dataset, the dataset is composed of delamination cases. So, the first task is to extract features from all of the delamination cases and then use these features as labels in the second step during model training. Therefore, in this step, the encoder and decoder parts of the proposed model are trained jointly, so the decoder part can be used separately for full wavefield predictions. During this step, the features are extracted with very minimal reconstruction error in a compressed form, which matches the dimensions of the latent space.
2. **Model training:** In this step, the actual model training is carried out. The full wavefield frames in a plate without delamination, along with the binary image of the respective delamination case, are fed into the DL model for training. The features extracted from encoder part of the first step are used as labels in this step, as shown in Figure 4.
3. **Evaluation of the proposed DL model on unseen data:** At this stage, both of the pretrained models (pretrained decoder from step 1 and pretrained encoder from step 2) are utilised for the prediction of the full wavefield frames on unseen data. During this step, the model just takes reference frames with the delamination information and produces the output as the full wavefield frames containing the interaction of Lamb waves with delamination.

The proposed ConvLSTM autoencoder model takes 32 frames as input concatenated with a binary image, which is replicated 32 times (see Figure 4). The DL model consists of six ConvLSTM layers (see Figure 5). The first ConvLSTM layer has 32 filters, the second and third layers have 192 filters, the fourth layer has 32 filters, and the last two ConvLSTM layers have 192 filters. The kernel size of the ConvLSTM layers was set to (3×3) with a stride of (1). The padding was set to "same", which makes the output the same as the input in the case of stride 1. Furthermore, a tanh (the hyperbolic tangent) activation function was used within the ConvLSTM layers that output values in a range between $(-1$ and $1)$. Maxpooling and upsampling were applied at each ConvLSTM layer for reducing the size of the features and the reconstruction purposes, respectively. Moreover, a batch normalisation technique [34] was applied at each of the ConvLSTM layers. At the final output layer, a 2D convolutional layer followed by a sigmoid activation function were applied.

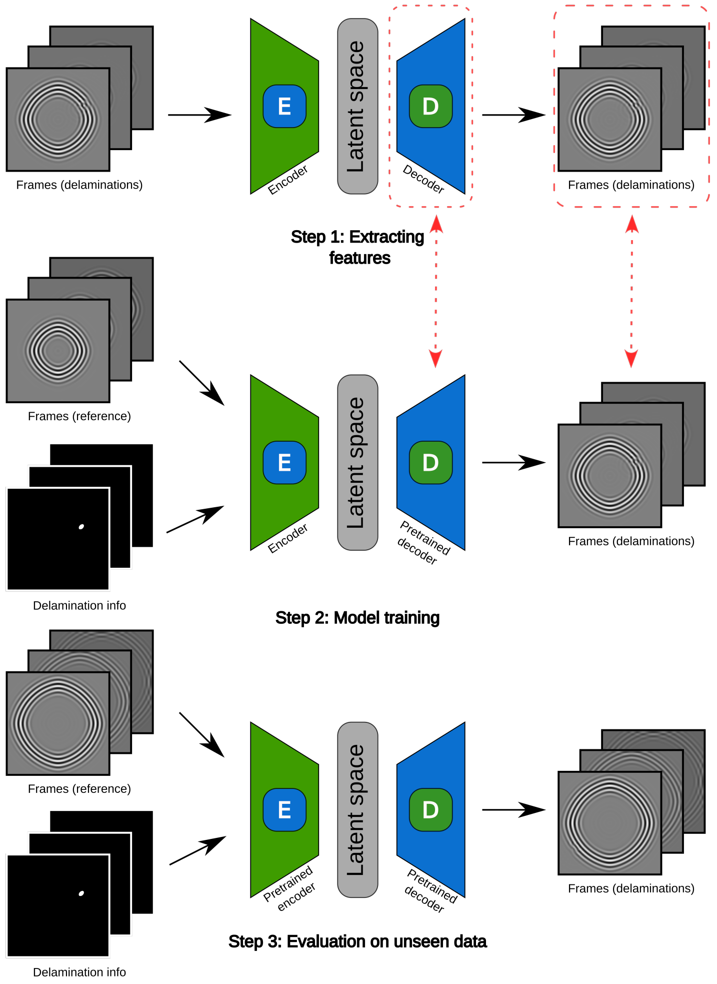

Figure 4. The flowchart of the proposed DL model.

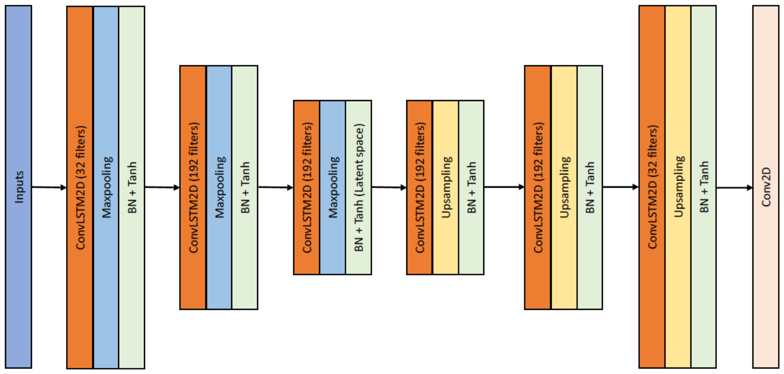

Figure 5. The architecture of the proposed ConvLSTM autoencoder model.

To alleviate the overfitting, we used an early-stopping mechanism that monitors the validation loss during the training of the model and stops the training of the model after 30 epochs if there is no improvement. The Adam optimiser was employed for backpropagation, and the MSE was used as a loss function for both training steps.

The peak signal-to-noise ratio (PSNR) metric values as a function of the epoch is shown in Figure 6. During both training and validation, these metrics converged. Moreover, the validation curve was slightly below the training curve, which indicates that overfitting did not occur.

The training was performed on a Nvidia Tesla V100 GPU. Each epoch took 4 min, and the model was trained on 142 epochs, so the proposed model took about 9.5 h for training.

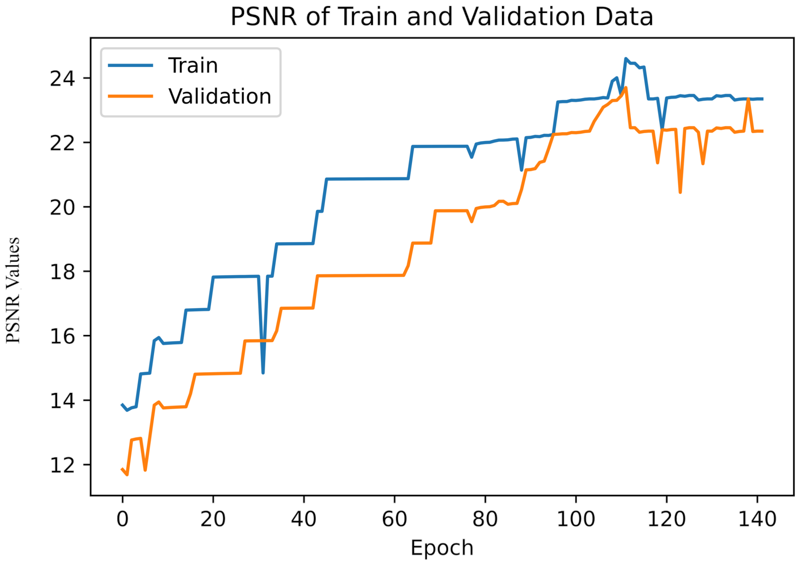

Figure 6. The training and validation PSNR metric as a function of the epoch.

For evaluating the performance of the proposed model, two evaluation metrics, namely the PSNR and Pearson correlation coefficient (Pearson CC), were utilised. The PSNR measures the maximum potential power of a signal and the power of the noise that affects the quality of its representation, and it is expressed mathematically in Equation (1):

$$PSNR = 20\log_{10}\frac{L}{\sqrt{MSE}}, \tag{1}$$

where L denotes the highest degree of variation present in the input image. Meanwhile, MSE stands for mean squared error, which represents the discrepancy between the predicted output and the relevant ground truth. The calculation of the MSE is shown in Equation (2):

$$MSE = \frac{1}{M*N}\sum_{M,N}\left(Y_{(m,n)} - \hat{Y}_{(m,n)}\right)^2, \tag{2}$$

where M and N represent the number of rows and columns in the input images, $Y_{(m,n)}$ is the ground truth value, and $\hat{Y}_{(m,n)}$ is the predicted value.

The Pearson CC is a metric that estimates the linear connection between two sets of variables, $\mathbf{x}$ (which represents the ground truth values) and $\mathbf{y}$ (which represents the predicted values). The mathematical formula for computing the Pearson CC is shown in Equation (3):

$$r_{xy} = \frac{\sum_{k=1}^{n}(x_k - \bar{x})(y_k - \bar{y})}{\sqrt{\sum_{k=1}^{n}(x_k - \bar{x})^2}\sqrt{\sum_{k=1}^{n}(y_k - \bar{y})^2}}, \tag{3}$$

where r_{xy} represents the Pearson CC, n represents the number of data points in a sample, and x_k and y_k denote the values of the ground truth and predicted values, respectively, for each data point. Additionally, $\bar{x}$ denotes the mean value of the sample, and $\bar{y}$ represents the mean value of the predicted values. The values of r_{xy} range from '−1' to '+1'. The value '0' specifies that there is no relation between the samples and the predicted values. A value greater than '0' indicates a positive relationship between the samples and the predicted data, whereas a value less than '0' represents a negative relationship between them.

The maximum PSNR and Pearson CC values on the validation data were noted as 23.7 dB and 0.99, respectively.

5. Inverse Method for Damage Identification

A global-best PSO algorithm implemented in Python was used in the optimisation process [35]. It takes a set of candidate solutions and tries to find the best solution using a position–velocity update method. It uses a star topology, where each particle is attracted to the best-performing particle. The algorithm follows two basic steps:

- The position update:

$$x_i(t+1) = x_i(t) + v_i(t+1), \tag{4}$$

- The velocity update:

$$v_{ij}(t+1) = w\, v_{ij}(t) + c_1\, r_{1j}(t)\, [y_{ij}(t) - x_{ij}(t)] + c_2\, r_{2j}(t)\, [\hat{y}_j(t) - x_{ij}(t)], \tag{5}$$

where r are random numbers, y_{ij} is the particle's best-known position, $\hat{y}_j$ is the swarm's best known position, c_1 is the cognitive parameter, c_2 is the social parameterm and w is the inertia parameter, which controls the swarm's movement. Cognitive and social parameters control the particle's behaviour when given two choices: (i) to follow its personal best or (ii) to follow the swarm's global best position. Overall, this dictates if the swarm is explorative or exploitative in nature. In our tests, we used the following parameters: $c_1 = c_2 = 0.3$ and $w = 0.8$. Good convergence was achieved for these sets of parameters; thus, further parameter tuning was unnecessary.

The following decision variables were used in the PSO:

- The delamination coordinates (x_c, y_c) with the bounds [0 mm, 500 m];
- A delamination elliptic shape represented by semimajor and semiminor axes a, b with the bounds [5 mm, 20 mm],
- A delamination rotation angle α with the bounds [0°, 180°].

Based on the decision variables, binary images of (256×256) pixels were generated (one image per particle—see Figure 1). In these images, ones (white pixels) represent delamination, whereas zeros (black pixels) represent healthy area.

The most important component of the proposed inverse method is the surrogate DL model described in Section 4. The trained DL model was used for ultrafast full wavefield prediction, as illustrated in Figure 1. Ultrafast means an evaluation duration below 1 s, which compares to computation times using FEM-based methods from 30 min to 1 h. For a single particle and respective binary image, the DL model was evaluated seven times for 32 consecutive frames, thus giving as an output 224 frames. These predicted frames were compared to the 'measured' frames by using the MSE metric, which was utilised in the objective function. However, for the sake of replicability of the results and the compatibility with the available dataset [31], we used synthetic data instead of measured data (acquired by the SLDV).

For each PSO iteration, the particles were updated according to Equations (4) and (5). The termination criterion was assumed as 100 iterations, but it was observed that the objective function value converged much faster. In the final step, the best-matching wavefields indicate the coordinates, and the semimajor and semiminor axis and rotation angles of the elliptic-shaped delamination. These parameters were used for a visual representation of the best-matched delamination in the form of a binary image compared against the ground truth (see also Figure 1).

As an evaluation metric for assessing the accuracy of the identified delamination, we used the intersection over union (IoU), which measures the degree to which the predicted delamination overlaps the true delamination. It is defined as follows:

$$IoU = \frac{Intersection}{Union} = \frac{\hat{Y} \cap Y}{\hat{Y} \cup Y}, \tag{6}$$

where $\hat{Y}$ is the predicted output, and Y is the ground truth (true delamination) in the form of binary images.

6. Results and Discussion

Separate evaluation was performed for theestimation of the accuracy of full wavefield predictions using the proposed surrogate DL model and for the estimation of the accuracy in delamination identification.

6.1. Evaluation of the Surrogate Dl Model

In this section, we present the evaluation of the proposed DL model based on the numerical test data of 95 delamination cases representing the frames of the full wavefield propagation, which was not shown in the proposed DL model during training. The proposed DL model was evaluated using numerical test data to demonstrate the capability to predict the interaction of Lamb waves with the delamination of various locations, shapes, and sizes.

Three different representative cases were selected from the numerical dataset to show the performance of the developed DL model. Figures 7–9 show three different frames from three selected numerical test cases. The frames on the left column represent the labels to which the prediction of the proposed DL model is compared. The frames on the right column represent the prediction using the DL model. Particular frames were selected to show the interaction of the propagating Lamb waves with the delamination, namely the 10th, 20th, and 30th frames after the interaction with the delamination. These frame numbers were easily extracted knowing the A0 mode velocity and the modelled delamination location.

As can be seen in the first scenario (Figure 7), the delamination occurred at the upper-left side of the plate; in the second scenario (Figure 8), the delamination occurred at the top left of the plate, whereas in the third scenario, (Figure 9) the delamination occurred at the top centre of the plate.

In all the presented cases (Figures 7–9), the change in the wave velocity due to delamination was well reproduced by the DL model. The wave reflections from the delamination were very well predicted in Figure 8, whereas in some cases and frames, the reflection pattern differed between the label and the DL prediction—compare Figure 9e,f. It should be underlined that these reflections were of much smaller amplitudes than the main wavefront, and the proposed DL model was not able to correctly reproduce all the detailed intricacies of the Lamb wave reflections. A more complex DL model could be required to further improve the results. Nevertheless, the testing results are satisfactory and very promising.

From all three scenarios, it can be confirmed that the proposed DL-based surrogate model has reconstructed the full wavefield containing delamination with minimal error. Furthermore, the PSNR and Pearson CC values of all three of these scenarios are shown in Table 1. The mean PSNR value was 21.8 dB, and the mean Pearson CC value was 0.98 on all of the test data. These values confirm that the predictions from the proposed DL model are accurate.

Table 1. DL surrogate model evaluation metrics for three numerical cases.

Scenario		PSNR	Pearson CC
First	10th frame	23.3 dB	0.96
	20th frame	23.4 dB	0.98
	30th frame	23.7 dB	0.98
Second	10th frame	21.4 dB	0.96
	20th frame	22.1 dB	0.98
	30th frame	22.6 dB	0.98
Third	10th frame	21.8 dB	0.97
	20th frame	22.1 dB	0.98
	30th frame	22.3 dB	0.99

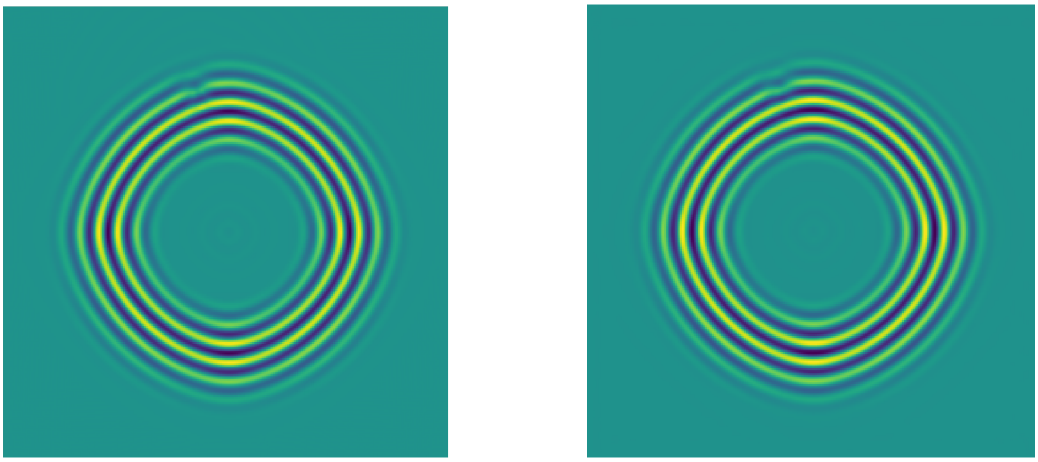

(**a**) Label: 10th frame (**b**) Prediction: 10th frame

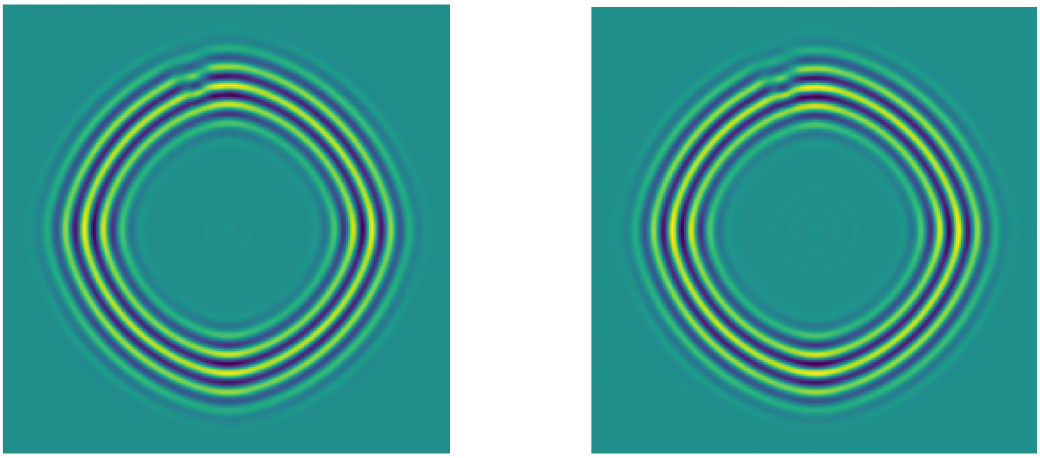

(**c**) Label: 20th frame (**d**) Prediction: 20th frame

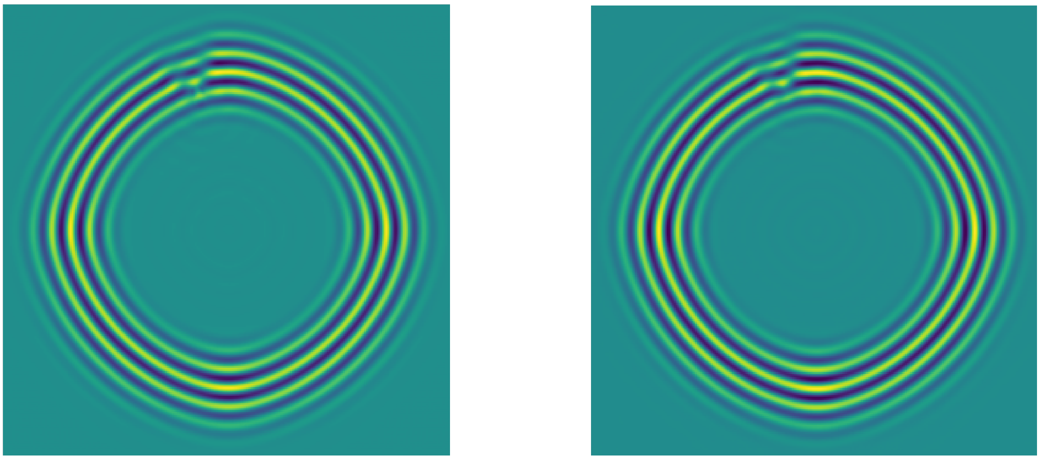

(**e**) Label: 30th frame (**f**) Prediction: 30th frame

Figure 7. First scenario: comparison of predicted frames with the label frames at 10th, 20th, and 30th frames after the interaction with delamination.

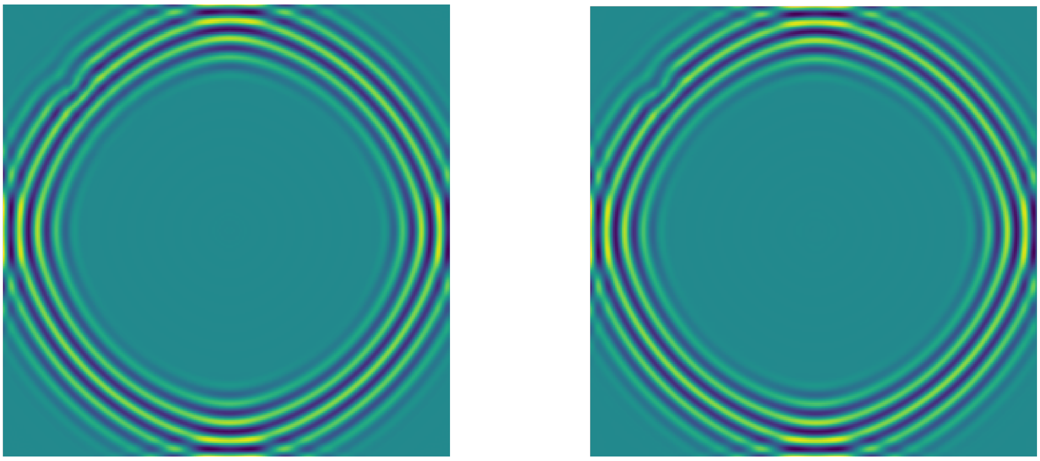

(**a**) Label: 10th frame (**b**) Prediction: 10th frame

(**c**) Label: 20th frame (**d**) Prediction: 20th frame

(**e**) Label: 30th frame (**f**) Prediction: 30th frame

Figure 8. Second scenario: comparison of predicted frames with the label frames at 10th, 20th, and 30th frames after the interaction with delamination.

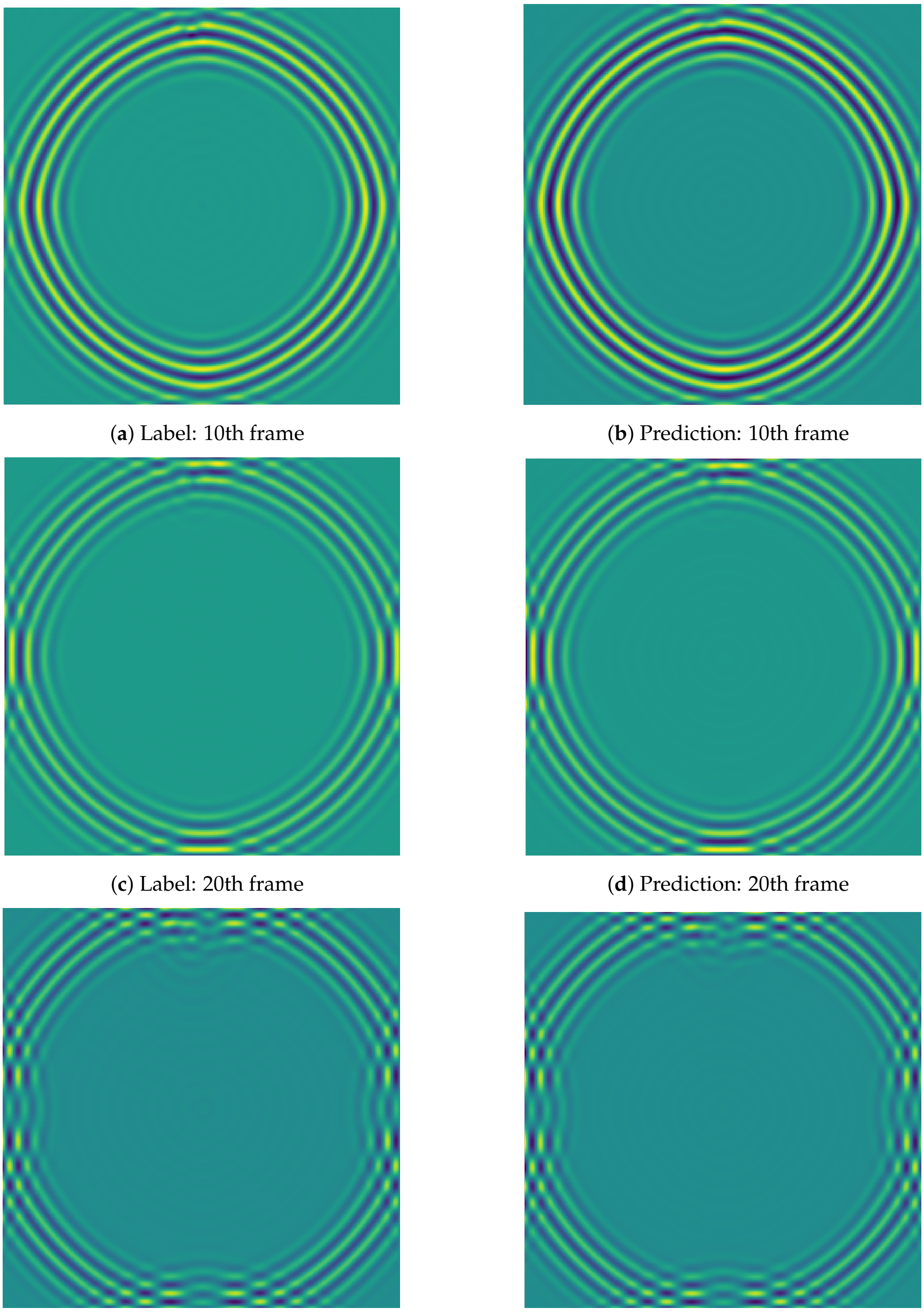
(**a**) Label: 10th frame (**b**) Prediction: 10th frame

(**c**) Label: 20th frame (**d**) Prediction: 20th frame

(**e**) Label: 30th frame (**f**) Prediction: 30th frame

Figure 9. Third scenario: comparison of predicted frames with the label frames at 10th, 20th, and 30th frames after the interaction with delamination.

6.2. Delamination Identification Results

The delamination identification results obtained by using PSO aided by the DL-based surrogate model are presented in Figure 10. Several runs were performed due to the metaheuristic nature of the PSO algorithm, and the results were selected for two runs for illustration purposes. The following cases were selected, namely case 1 (Figure 10a,b), case 2 (Figure 10c,d), and case 3 (Figure 10e,f), where the damage identification difficulty can be ranked from highest to lowest. The most difficult case was case 1, in which the delamination was in the corner of the plate. The delamination for case 2 was located very close to the top edge of the plate, where edge reflections can overshadow reflections from delamination. The delamination for case 3 was quite large and far away from the plate's edges, so it should have been easily detected.

Actually, the damage identification difficulty level is reflected in the obtained IoU values, which are shown in the zoomed-in regions around the delamination in Figure 10. On average, the lowest IoU values were obtained for case 1.

The visualisation of the damage identification results has been performed in such a way that the delamination ground truth is shown in the green colour, the DL model prediction is shown in the red colour, and the intersection of the two has been made by colour mixing, which gives the yellow colour. Therefore, the more yellow pixels there are, the greater the overlap of the delaminations and, in turn, the better the accuracy.

It should be noted that despite the low IoU values in certain cases, the identification algorithm performed remarkably well, because the delamination was localised accurately for each scenario.

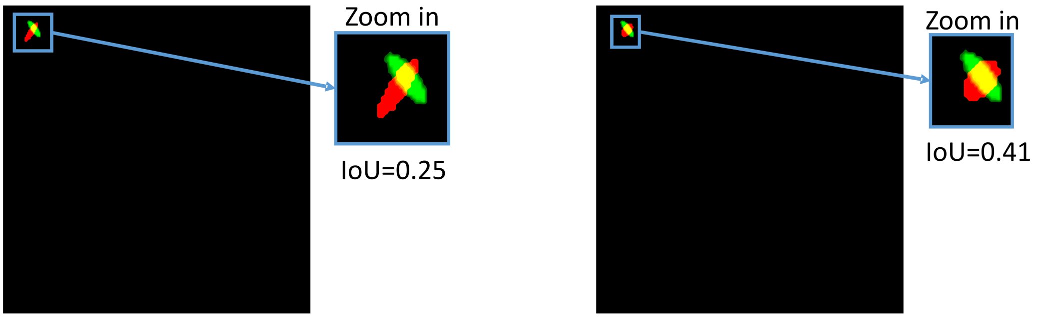

(**a**) Case 1: run 1 (**b**) Case 1: run 2

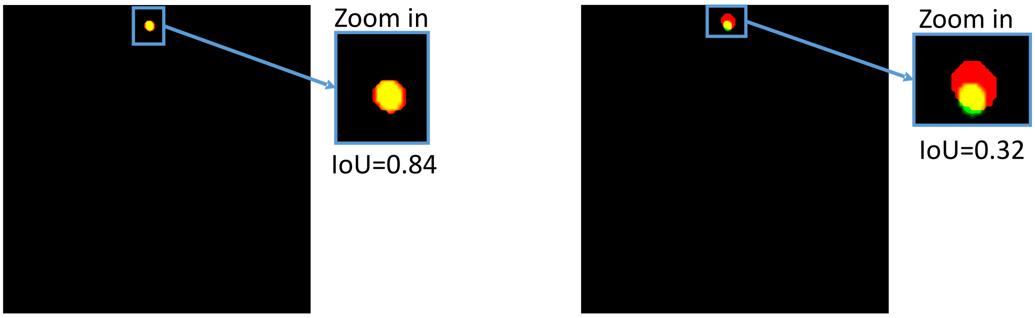

(**c**) Case 2: run 1 (**d**) Case 2: run 2

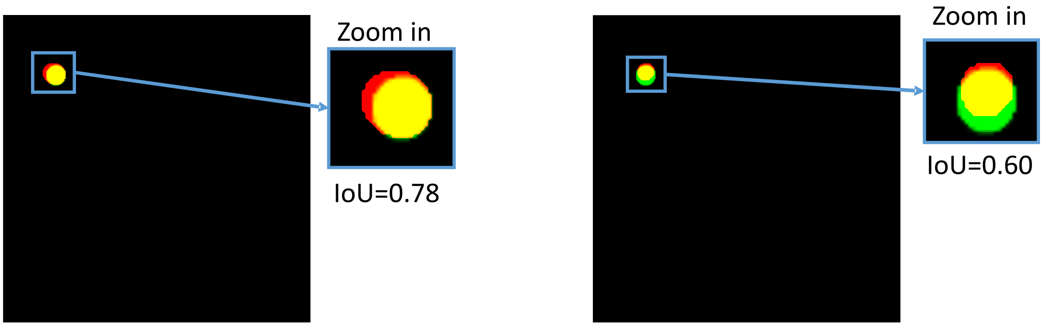

(**e**) Case 3: run 1 (**f**) Case 3: run 2

Figure 10. Delamination identification results: green—ground truth, red—prediction, yellow—intersection.

The delamination identification results in terms of the IoU values are gathered in Table 2, wherein we also find the results from [11], which have been added for comparison.

The method presented in [11] is completely different from the one presented here, but it relies on the same dataset. However, the frame size was larger, namely (512 × 512) pixels versus (256 × 256) pixels here, thus giving a better resolution of the damage identification.

Although, according to Table 2, the current results are not as good as compared to our previous paper [11], the advantage of the proposed method is that it can be easily extended to cases in which only a limited number of signals are available in comparison to full wavefield data. This is extremely important for practical applications in structural health monitoring where only the signals at sensor locations are available.

It should also be stressed that the complexity of the proposed DL model and the dataset size used for training are limited by the memory of a single Nvidia Tesla V100 GPU (32 GB memory), which was available to us. Certainly, the surrogate DL model can be improved by using a larger number of frames in the sequence of ConvLSTM layers. It is expected that the damage identification would improve as well with a more accurate surrogate DL model.

Table 2. Damage identification evaluation metrics for three numerical cases.

Case Number		**IoU**	
		Current	**[11]**
1	run 1	0.25	0.74
	run 2	0.41	
	run 3	0.34	
2	run 1	0.84	0.76
	run 2	0.32	
	run 3	0.34	
3	run 1	0.78	0.88
	run 2	0.60	
	run 3	0.85	

7. Conclusions and Future Work

In this research work, we presented a novel DL-based surrogate model. The developed model adopts the architecture of the autoencoder–decoder in conjunction with the ConvLSTM algorithm for the prediction of a full wavefield containing interacting Lamb waves with delamination. In the proposed model, the encoder and decoder parts were trained jointly on a synthetic dataset consisting of frames, which contain wave patterns of the delamination reflections and changes in the wavefront due to delamination. Then, the encoder was trained separately on reference data without delamination. The delamination information in the form of binary images has also been provided, along with the reference images to the encoder part for training the encoder and the final prediction of the frames propagating in the plate with delamination. In simple words, this DL-based surrogate model takes the full wavefield frames of propagating waves in a healthy plate as input and predicts full wavefields in a plate that contains single delamination.

The proposed DL model performed well, as was proven by the results. The proposed DL model is helpful for the prediction of the full wavefield data from the time of excitation initiation to the desired simulation time. The predicted wavefield from the proposed architecture can be used for inverse problems in NDT (shown here) and SHM (possibly in the future). The wavefield prediction using the proposed DL model is ultrafast; therefore, objective functions, which require multiple evaluations, can be applied in the inverse methods. In contrast, such an approach is unfeasible using conventional forward solvers, e.g., based on p-FEM or SEM.

It should be noted, however, that the generalisation capabilities of the applied DL model highly depend on the dataset provided for training. The method was tested only on one type of CFRP layup and on one type of excitation signal. For the real case scenario, the DL model should be trained considering the complexity of the inspected structure such as the stiffeners and material properties. Therefore, the initial computational effort is high in comparison to data-driven-only approaches.

It is planned to test the proposed damage identification framework on experimental data in the future.

Author Contributions: Conceptualisation, S.U. and P.K.; methodology, S.U. and P.K.; software, S.U., P.K., and A.A.I.; validation, S.U. and A.A.I.; formal analysis, P.K.; investigation, S.U.; resources, P.K.; data curation, A.A.I.; writing—original draft preparation, S.U. and P.K.; writing—review and editing, E.C. and W.O.; visualisation, S.U. and P.K.; supervision, P.K.; project administration, W.O.; funding acquisition, W.O. and E.C. All authors have read and agreed to the published version of the manuscript.

Funding: The research was funded by the Polish National Science Centre under grant agreements no 2019/01/Y/ST8/00060.

Institutional Review Board Statement: Not applicable

Informed Consent Statement: Not applicable

Data Availability Statement: The dataset is made available online at https://doi.org/10.5281/zenodo.5414555 (accessed on 3 September 2021) so that the results can be easily replicated. See also reference [31].

Conflicts of Interest: The authors declare no conflicts of interest.

References

1. Staszewski, W.J.; Mahzan, S.; Traynor, R. Health monitoring of aerospace composite structures—Active and passive approach. *Compos. Sci. Technol.* **2009**, *69*, 1678–1685. [CrossRef]
2. Tuo, H.; Lu, Z.; Ma, X.; Xing, J.; Zhang, C. Damage and failure mechanism of thin composite laminates under low-velocity impact and compression-after-impact loading conditions. *Compos. Part Eng.* **2019**, *163*, 642–654. [CrossRef]
3. Tian, Z.; Yu, L.; Leckey, C. Delamination detection and quantification on laminated composite structures with Lamb waves and wavenumber analysis. *J. Intell. Mater. Syst. Struct.* **2015**, *26*, 1723–1738. [CrossRef]
4. Munian, R.K.; Mahapatra, D.R.; Gopalakrishnan, S. Lamb wave interaction with composite delamination. *Compos. Struct.* **2018**, *206*, 484–498. [CrossRef]
5. Barthorpe, R.J.; Worden, K. Emerging Trends in Optimal Structural Health Monitoring System Design: From Sensor Placement to System Evaluation. *J. Sens. Actuator Netw.* **2020**, *9*, 31. [CrossRef]
6. Ihn, J.B.; Chang, F.K. Pitch-catch active sensing methods in structural health monitoring for aircraft structures. *Struct. Health Monit.* **2008**, *7*, 5–19. [CrossRef]
7. Cantero-Chinchilla, S.; Chiachío, J.; Chiachío, M.; Chronopoulos, D.; Jones, A. Optimal sensor configuration for ultrasonic guided-wave inspection based on value of information. *Mech. Syst. Signal Process.* **2020**, *135*, 106377 . [CrossRef]
8. Radzieński, M.; Kudela, P.; Marzani, A.; De Marchi, L.; Ostachowicz, W. Damage identification in various types of composite plates using guided waves excited by a piezoelectric transducer and measured by a laser vibrometer. *Sensors* **2019**, *19*, 1958. [CrossRef] [PubMed]
9. Girolamo, D.; Chang, H.Y.; Yuan, F.G. Impact damage visualization in a honeycomb composite panel through laser inspection using zero-lag cross-correlation imaging condition. *Ultrasonics* **2018**, *87*, 152–165. [CrossRef]
10. Rogge, M.D.; Leckey, C.A. Characterization of impact damage in composite laminates using guided wavefield imaging and local wavenumber domain analysis. *Ultrasonics* **2013**, *53*, 1217–1226. [CrossRef]
11. Ullah, S.; Ijjeh, A.A.; Kudela, P. Engineering Applications of Artificial Intelligence Deep learning approach for delamination identification using animation of Lamb waves. *Eng. Appl. Artif. Intell.* **2023**, *117*, 105520. [CrossRef]
12. Duczek, S.; Gabbert, U. Anisotropic hierarchic finite elements for the simulation of piezoelectric smart structures. *Eng. Comput.* **2013**, *30*, 682–706. [CrossRef]
13. Anitescu, C.; Nguyen, C.; Rabczuk, T.; Zhuang, X. Isogeometric analysis for explicit elastodynamics using a dual-basis diagonal mass formulation. *Comput. Methods Appl. Mech. Eng.* **2019**, *346*, 574–591. [CrossRef]
14. Mossaiby, F.; Joulaian, M.; Düster, A. The spectral cell method for wave propagation in heterogeneous materials simulated on multiple GPUs and CPUs. *Comput. Mech.* **2019**, *63*, 805–819. [CrossRef]
15. Kudela, P.; Moll, J.; Fiborek, P. Parallel spectral element method for guided wave based structural health monitoring. *Smart Mater. Struct.* **2020**, *29*, 095010. [CrossRef]
16. Willberg, C.; Duczek, S.; Vivar Perez, J.M.; Schmicker, D.; Gabbert, U. Comparison of different higher order finite element schemes for the simulation of Lamb waves. *Comput. Methods Appl. Mech. Eng.* **2012**, *241–244*, 246–261. [CrossRef]
17. Zhang, E.; Dao, M.; Karniadakis, G.E.; Suresh, S. Analyses of internal structures and defects in materials using physics-informed neural networks. *Sci. Adv.* **2022**, *8*, eabk0644. [CrossRef] [PubMed]

18. Jin, H.; Zhang, E.; Espinosa, H.D. Recent Advances and Applications of Machine Learning in Experimental Solid Mechanics: A Review. *Appl. Mech. Rev.* **2023**, *75*, 061001. [CrossRef]
19. Rautela, M.; Gopalakrishnan, S. Deep learning frameworks for wave propagation-based damage detection in 1d-waveguides. In Proceedings of the 11th International Symposium on NDT in Aerospace, Saclay, France, 15 November 2019; Volume 2, pp. 1–11.
20. Pandey, P.; Rai, A.; Mitra, M. Explainable 1-D convolutional neural network for damage detection using Lamb wave. *Mech. Syst. Signal Process.* **2022**, *164*, 108220. [CrossRef]
21. Ijjeh, A.A.; Kudela, P. Deep learning based segmentation using full wavefield processing for delamination identification: A comparative study. *Mech. Syst. Signal Process.* **2022**, *168*, 108671. [CrossRef]
22. Pinaya, W.H.L.; Vieira, S.; Garcia-Dias, R.; Mechelli, A. Autoencoders. In *Machine Learning*; Elsevier: Amsterdam, The Netherlands, 2020; pp. 193–208.
23. Ardelean, E.R.; Coporîie, A.; Ichim, A.M.; Dînșoreanu, M.; Mureșan, R.C. A study of autoencoders as a feature extraction technique for spike sorting. *PLoS ONE* **2023**, *18*, e0282810. [CrossRef] [PubMed]
24. Simpson, T.; Dervilis, N.; Chatzi, E. Machine learning approach to model order reduction of nonlinear systems via autoencoder and LSTM networks. *J. Eng. Mech.* **2021**, *147*, 04021061. [CrossRef]
25. Shi, X.; Chen, Z.; Wang, H.; Yeung, D.Y.; Wong, W.K.; Woo, W.c. Convolutional LSTM network: A machine learning approach for precipitation nowcasting. *Adv. Neural Inf. Process. Syst.* **2015**, *28*.
26. Jo, S.; Park, C.; Ryu, D.W.; Ahn, S. Adaptive surrogate estimation with spatial features using a deep convolutional autoencoder for CO_2 geological sequestration. *Energies* **2021**, *14*, 413. [CrossRef]
27. Nikolopoulos, S.; Kalogeris, I.; Papadopoulos, V. Non-intrusive surrogate modeling for parametrized time-dependent partial differential equations using convolutional autoencoders. *Eng. Appl. Artif. Intell.* **2022**, *109*, 104652. [CrossRef]
28. Peng, H.; Yan, J.; Yu, Y.; Luo, Y. Structural surrogate model and dynamic response prediction with consideration of temporal and spatial evolution: An encoder–decoder ConvLSTM network. *Int. J. Struct. Stab. Dyn.* **2021**, *21*, 2150140. [CrossRef]
29. Zargar, S.A.; Yuan, F.G. Impact diagnosis in stiffened structural panels using a deep learning approach. *Struct. Health Monit.* **2021**, *20*, 681–691. [CrossRef]
30. Keneddy, J.; Eberhart, R.C. Particle Swarm Optimization. In Proceedings of the Proceedings of the IEEE International Joint Conference on Neural Networks, Perth, WA, Australia, 27 November–1 December 1995; pp. 1942–1948.
31. Kudela, P.; Ijjeh, A. Synthetic Dataset of a Full Wavefield Representing the Propagation of Lamb Waves and Their Interactions with Delaminations. 2021. Available online: https://zenodo.org/records/5414555 (accessed on 3 September 2021).
32. Geuzaine, C.; Remacle, J.F. Gmsh: A 3-D finite element mesh generator with built-in pre- and post-processing facilities. *Int. J. Numer. Methods Eng.* **2009**, *79*, 1309–1331. [CrossRef]
33. Szegedy, C.; Liu, W.; Jia, Y.; Sermanet, P.; Reed, S.; Anguelov, D.; Erhan, D.; Vanhoucke, V.; Rabinovich, A. Going deeper with convolutions. In Proceedings of the IEEE Conference on Computer Vision and Pattern Recognition, Boston, MA, USA, 7–12 June 2015; pp. 1–9.
34. Santurkar, S.; Tsipras, D.; Ilyas, A.; Madry, A. How does batch normalization help optimization? In Proceedings of the Advances in Neural Information Processing Systems, Montreal, QC, Canada, 3–8 December 2018; Volume 2018, pp. 2483–2493. [CrossRef]
35. Miranda Lester James, V.; Moser, A.; Cronin, S.K. PYSWARMS a research toolkit for Particle Swarm Optimization in Python. *J. Open Source Softw.* **2018**, *3*, 433. [CrossRef]